Journal of The Electrochemical Society, **160** (5) A3108-A3112 (2013)
0013-4651/2013/160(5)/A3108/5/$31.00 © The Electrochemical Society

JES Focus Issue on Intercalation Compounds for Rechargeable Batteries

Synthesis of Lithium and Manganese-Rich Cathode Materials via an Oxalate Co-Precipitation Method

Dapeng Wang,[a,b] Ilias Belharouak,[a,*,z] Guangwen Zhou,[b] and Khalil Amine[a,*]

[a]*Chemical Sciences and Engineering Division, Argonne National Laboratory, Argonne, Illinois 60439, USA*
[b]*State University of New York at Binghamton, Binghamton, New York 13902, USA*

The synthesis of Li- and Mn- rich cathode materials with oxalate co-precipitation method was comprehensively investigated. Thermodynamic calculation and advanced characterizations were conducted to study the effects of reaction pH and precipitation agent on the morphology and composition of the precipitates. It was found that manganese oxalate has a higher solubility compared to nickel oxalate, especially at low reaction pH. In addition, the different capability of Ni^{2+} and Mn^{2+} to form transition metal ammonia complexes led to a composition discrepancy in the precipitation. The desired nickel manganese oxalate precursor composition could only be achieved when these factors were considered, and cathode materials synthesized based on this precursor exhibited satisfactory electrochemical performance (about 220 mAh · g^{-1} over 70 cycles under C/10 rate).
© 2013 The Electrochemical Society. [DOI: 10.1149/2.016305jes] All rights reserved.

Manuscript submitted December 31, 2012; revised manuscript received February 7, 2013. Published March 20, 2013. *This paper is part of the JES Focus Issue on Intercalation Compounds for Rechargeable Batteries.*

At present, lithium- and manganese- rich oxide materials are attracting extensive research interest due to their low cost, high capacity and high energy density for lithium batteries.[1–6] In these composites, it is widely accepted that short-range-order Li_2MnO_3-like nanodomains exist within the layered $R\bar{3}m$ structural component.[3,7–15] The excess lithium in the composite structure can inhibit the Li and Ni cationic exchange between the layers, and hence improves the overall electrochemical performance.[16] The improvement is, however, linked to the synthesis method by which these materials can be produced.[1–10,17–21] Of interest, co-precipitation reactions based on hydroxide and carbonate processes have been widely used for the production of chemically homogenous precursors and, thus, highly performing cathodes.[17–21] The main advantages of these co-precipitation methods can be summarized in the following points: (1) low cost of the starting raw materials (usually transition metal sulfates); (2) high solubility of the starting raw chemicals in contrast to extremely low solubility of the precipitates; (3) wide solid solution ranges of transition metal precipitates; and (4) facile morphology and particle size distribution control.[17–21] Both carbonate and hydroxide co-precipitation methods have been widely studied by our group[17–21] and other researchers.[22–24] The major difficulties encountered during the development of these two methods were: for the carbonate process; (i) continuous growth of secondary particles and ring morphology which can lead to undesired electrochemical performance,[21] and (ii) the high specific surface area which renders the precursors vulnerable to moisture and makes it difficult to lithiate with the right amount of lithium salts;[19] and for the hydroxide process, (i)' Mn^{2+} can easily be oxidized to Mn^{3+} or Mn^{4+}, and (ii)' the difficulty in controlling the morphology of the Mn-rich hydroxide precursors. As a consequence, the oxalate co-precipitation is being considered as an alternative process since Mn^{2+} and Ni^{2+} cations form a continuous solid solution and are both stable in the oxalate matrix, and also because the transition metals oxalates are produced in a saturated hydrated form. However, we found that the solubility of manganese and nickel oxalates strongly depends on the reaction pH and chelating agents. In this research, the effects of reaction pH and ammonia on morphology, structure, and composition of the nickel manganese oxalate precipitates and the resulting cathodes were extensively studied in order to establish the chemical fundamentals for the oxalate co-precipitation method as a route for producing high capacity cathodes.

Experiments

Nickel sulfate hexahydrate ($NiSO_4 \cdot 6H_2O$), manganese sulfate monohydrate ($MnSO_4 \cdot H_2O$), oxalic acid dehydrate ($H_2C_2O_4 \cdot H_2O$), ammonium hydroxide ($NH_3 \cdot H_2O$), and sodium hydroxide (NaOH) were used as the starting materials to prepare $Ni_{0.25}Mn_{0.75}C_2O_4 \cdot 2H_2O$ precursor. The experimental setup is shown in Figure 1. Transition metal sulfate solution (1M, 25% nickel sulfate and 75% manganese sulfate), oxalic acid solution (1M), and basic solution (1M, sodium hydroxide or ammonium hydroxide) were pumped into a beaker reactor kept at 80°C. The feeding rates of the transition metal sulfate solution and the oxalic acid solution were calibrated to be 0.5 L/hr. The flow rate of the basic solution was controlled by a pH controller. The collected precipitates were filtrated by vacuum filtration and vacuum dried at 100°C for over 12 hours. The oxalate precursor powder was thoroughly mixed with a suitable amount of Li_2CO_3 and calcined at 900°C in air for 14 hr.

The electrochemical properties of the materials were evaluated in CR-2032 type cells. The cathode was made of 80% active material, 10% acetylene black, and 10% polyvinylidene difluoride (PVDF) binder coated onto an aluminum foil. Cells were assembled inside a helium-filled glove box with lithium metal as the counter anode. Celgard 2325 membrane was used as the separator. The electrolyte was 1.2M $LiPF_6$ dissolved in ethylene carbonate (EC) and ethyl methyl carbonate (EMC) (3:7 vol.%). The cells were tested in the voltage range of 2.0–4.6 V at room temperature.

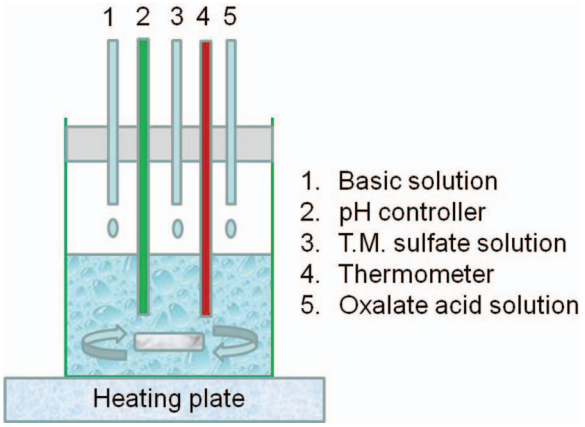

Figure 1. Schematic setup of the co-precipitation system.

*Electrochemical Society Active Member.
[z]E-mail: belharouak@anl.gov

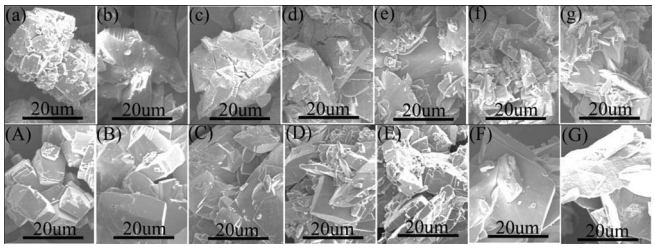

Figure 2. SEM images of oxalate precursors synthesized under different conditions: (a)-(g), ammonia used to adjust pH from 1 to 7; (A)-(G), NaOH used to adjust pH from 1 to 7.

The precursor and cathode material morphology were characterized with a cold field emission scanning electron microscopy (SEM, Hitachi S-4700-II), and the composition was assessed by inductively coupled plasma-mass spectroscopy (ICP-MS). The $Ni_{0.25}Mn_{0.75}C_2O_4 \cdot 2H_2O$ chemical formula and crystal structure were confirmed with Fourier transform infrared spectroscopy (FTIR), thermal gravimetrical analysis-differential scanning calorimetry (TGA-DSC), and a D5000 Siemens X-ray diffractometer (XRD) using a Cu-Kα radiation source (λ = 1.5406 Å). For the XRD, the samples were scanned from 2θ = 5 to 80° at a scan rate of 20 s per 0.02°. The phase purity of the cathode materials was verified with high energy synchrotron XRD conducted at Sector 11-ID-C (wavelength is 0.107805 Å) of the Advanced Photon Source (APS) at Argonne National Laboratory.

Results and Discussion

Figure 2 shows the morphology evolution when the reaction pH was gradually increased from 1 to 7. Figures 2a through 2g correspond to precipitates synthesized at pH 1 to pH 7, with ammonium hydroxide as the pH control solution. Figures 2A to 2G correspond to precipitates collected under different pH with NaOH as the pH control. When the pH was increased from 1 to 7 through ammonium hydroxide addition, the particles gradually transformed from cubic to a lamellar morphology. The particle size distribution was broad, with small particles less than 1 μm and large particles greater than 30 μm. When NaOH was used to adjust the pH, the particles became more regular in shape and had narrow distribution between 10 and 20 μm.

The solubility dependence of $MnC_2O_4 \cdot 2H_2O$ and $NiC_2O_4 \cdot 2H_2O$ on pH can be theoretically calculated based on the equilibrium equations in Table I. The calculations show that when NaOH is used as the pH regulator, the Mn^{2+} and Ni^{2+} concentration in the solution has the following dependence on pH:

$$[Mn^{2+}] = 0.251 \times 10^{-PH} \quad [1]$$

$$[Ni^{2+}] = 0.067 \times 10^{-PH} \quad [2]$$

Equations 1 and 2 indicate the following: (1) at the same reaction pH, $MnC_2O_4 \cdot 2H_2O$ has four times higher solubility than $NiC_2O_4 \cdot 2H_2O$, and (2) $[Mn^{2+}]$ and $[Ni^{2+}]$ decrease exponentially as pH increases (Figure 3a).

Table I. Equilibrium reactions and constants used in calculation.

Equilibrium reactions	Equilibrium constant K
$H_2C_2O_4 \leftrightarrow H^+ + HC_2O_4^-$	5.6×10^{-2}
$HC_2O_4^- \leftrightarrow H^+ + C_2O_4^{2-}$	5.1×10^{-5}
$MnC_2O_4 \leftrightarrow Mn^{2+} + C_2O_4^{2-}$	1.7×10^{-7}
$NiC_2O_4 \leftrightarrow Ni^{2+} + C_2O_4^{2-}$	7.8×10^{-10}
$Mn^{2+} + nNH_3 \leftrightarrow [Mn(NH_3)_n]^{2+}$	See Ref.16
$Ni^{2+} + nNH_3 \leftrightarrow [Ni(NH_3)_n]^{2+}$	See Ref.16
$NH_3 \bullet H_2O \leftrightarrow NH_4^+ + OH^-$	5.7×10^{-10}
$H_2O \leftrightarrow OH^- + H^+$	10^{-14}

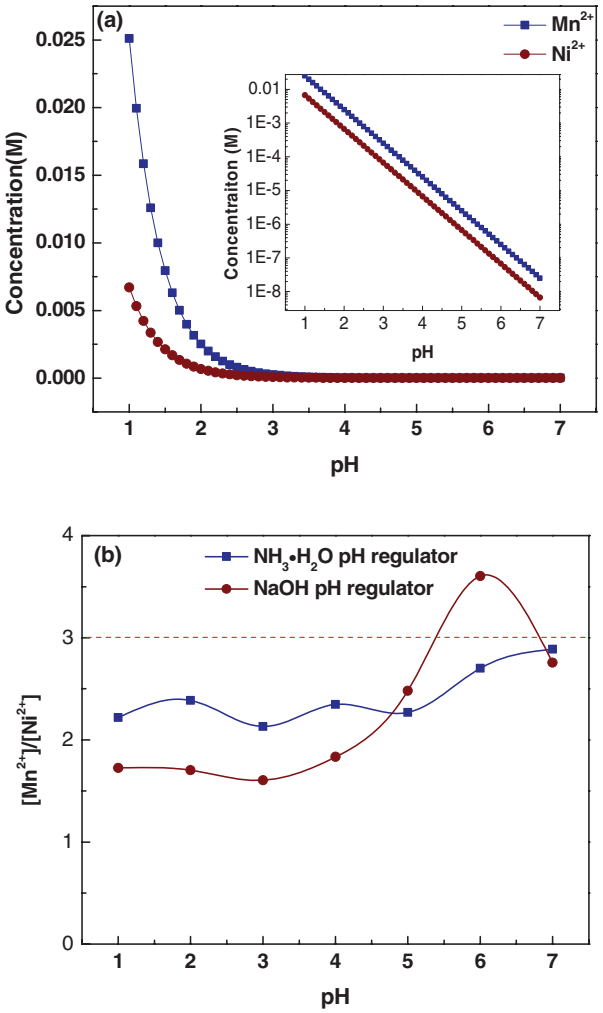

Figure 3. (a) Theoretically calculated Ni and Mn ion concentrations in the solution. (b) ICP-MS measured Ni/Mn atomic ratio in the precipitation as a function of reaction pH.

Figure 3b show the reaction pH and ammonia effects on the precipitate chemical compositions. The ideal [Mn]/[Ni] atomic ratio measured with ICP-MS is plotted as a reference (horizontal dashed line) (Figure 3b). The ICP-MS analysis showed that when ammonia was used as the pH regulator, the [Mn]/[Ni] atomic ratio increased slowly from 2.2 to 2.9 with the increase of pH from 1 to 7. When NaOH was used to increase pH from 1 to 7, the [Mn]/[Ni] first increased from 1.7 to 3.5, then dropped quickly to 2.8 at pH 7. The sharp drop of [Mn]/[Ni] when pH was increased from 6 to 7 may relate to the formation of $Ni(OH)_2$, which can increase the Ni concentration in the precipitate. Ideally, the [Mn]/[Ni] in the precipitate should be close to that in the feeding solution, which is 3 in these experiments. The deviation of precipitate composition is caused by solubility differences between nickel oxalate and manganese oxalate. The solubility of $MnC_2O_4 \cdot 2H_2O$ and $NiC_2O_4 \cdot 2H_2O$ are 0.0309 g and 0.0118 g, respectively, at 25°C.[25] The [Mn] and [Ni] did not change much when the reaction pH was tuned by ammonia. The residual Ni and Mn concentrations in the supernatant were measured with ICP-MS as shown in Figure 4. Based on the results shown in Figure 4a, the fluctuations of [Mn] and [Ni] were within one order of magnitude, and the variation in [Ni] is slightly larger than that of [Mn] in the recovered solutions after filtration. This difference is attributed to the fact that pH has a greater effect on the formation of complexes between Ni^{2+} and

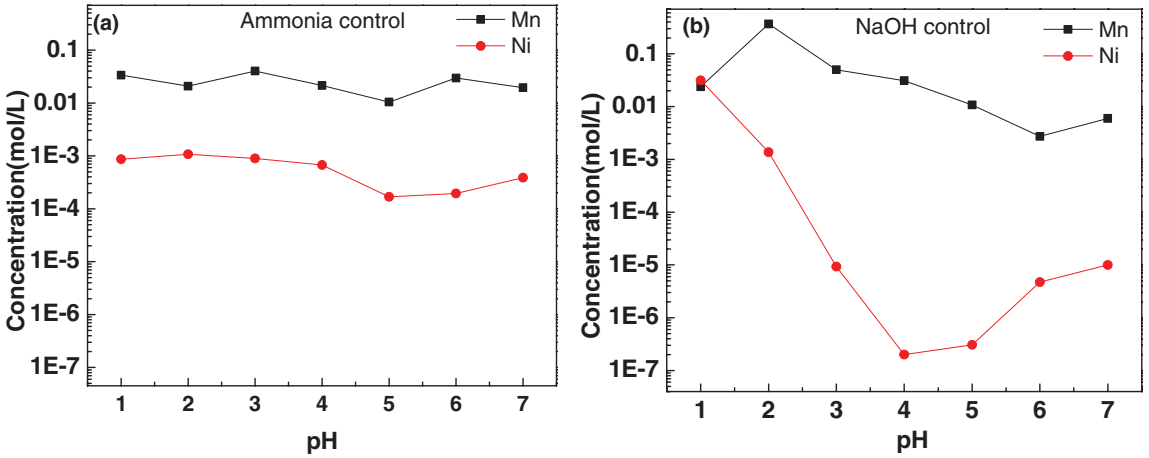

Figure 4. ICP-MS measured Ni and Mn concentration as a function of reaction pH with pH regulator of (a) ammonia and (b) NaOH.

ammonia than that between Mn^{2+} and ammonia. However, when NaOH solution was used to regulate the pH from 1 to 7, [Ni] underwent a dramatic decrease from 10^{-2} to 10^{-7} mol/L, while the change in [Mn] was still within two orders of magnitude (Figure 4b). Combining the SEM and ICP-MS results, we concluded that the ammonium complexes can sustain a relatively high and stable [Ni] and [Mn] in the solution, regardless of the pH. This stable Ni^{2+} and Mn^{2+} source can ensure a constant supersaturation during the whole synthesis; thus, inefficiency in mixing would not significantly affect the nucleation and growth processes. The relatively high ion concentrations can also create a homogeneous nucleation environment during the entire synthesis, leading to relatively small precipitate particle sizes.

Except for the composition, the phase purity of the oxalate precipitate is another critical factor for the cathode material synthesis. Manganese oxalates could be precipitated as $MnC_2O_4 \cdot 2H_2O$, $MnC_2O_4 \cdot 3H_2O$, and $Mn_2(C_2O_4)(OH)_2$ when synthesis conditions are changed.[26] The $MnC_2O_4 \cdot 2H_2O$ is a monoclinic structured white powder; $Mn_2(C_2O_4)(OH)_2$ is also monoclinic but belongs to $P2_1/c$ space group; and $MnC_2O_4 \cdot 3H_2O$ is an orthorhombic structured pink powder. In this study, all the precipitates appear to be light green, indicating a monoclinic di-hydrate structure. This color is attributed to $NiC_2O_4 \cdot 2H_2O$.

As shown in Figure 3b and Figure 4a, ammonia can serve as pH buffer, ensuring a nearly pH independent transition metal concentration in the solution. Ammonia is used instead of sodium hydroxide as pH regulator for all the reactions mentioned in the following discussion. The XRD patterns of the oxalate precipitates synthesized at pH 1 to pH 7 are assembled in Figure 5. Shown for comparison are the $MnC_2O_4 \cdot 2H_2O$[27] and $NiC_2O_4 \cdot 2H_2O$[28] standard diffraction patterns. The synthesized materials are isostructural to manganese oxalate, and no nickel oxalate impurity peaks were detected within the accuracy of the lab X-ray diffractometer, suggesting a single-phase solid solution. This observation is consistent with the reports that nickel oxalate and manganese oxalate could form solid solutions when the Ni/(Ni + Mn) atomic ratio is in the range of 0.16 to 0.33.[29]

The FTIR spectroscopic results of the oxalate precursor are shown in Figure 6. The bands at 1316 and 1358 cm^{-1} can be assigned to O–C–O symmetric stretches, and the band at 1615 cm^{-1} is the result of asymmetric stretches. The bands at 786 and 488 cm^{-1} are related to the C=C–O and O–C–O bending vibrations, respectively. The broad band at 3374 cm^{-1} is the fingerprint of hydration in the collected powder. These observations are consistent with reports from previous literature concerned with $MnC_2O_4 \cdot 2H_2O$.[30]

Figure 7 shows the TGA-DSC results obtained with N_2 as both a protective cover gas and purge gas and a heating rate of 5 K/min. No weight loss was observed at temperatures lower than 200°C, meaning the powder was completely dry and had no absorbed moisture. This characteristic is beneficial to the later lithiation, in which precise

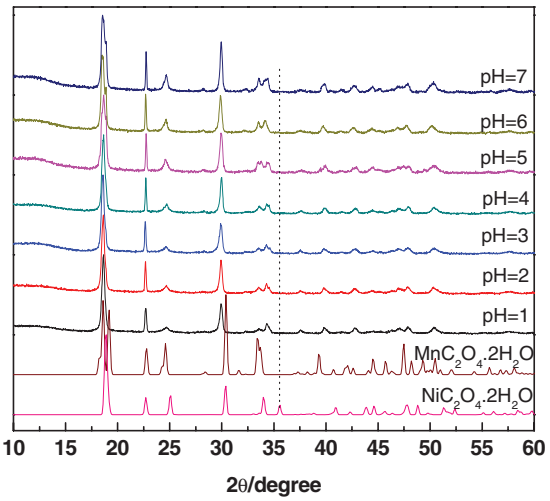

Figure 5. XRD patterns of oxalate precursors synthesized at pH 1 to pH 7 with ammonia as the regulator. Shown for comparison are the $MnC_2O_4 \cdot 2H_2O$[23] and $NiC_2O_4 \cdot 2H_2O$[24] standard diffraction patterns.

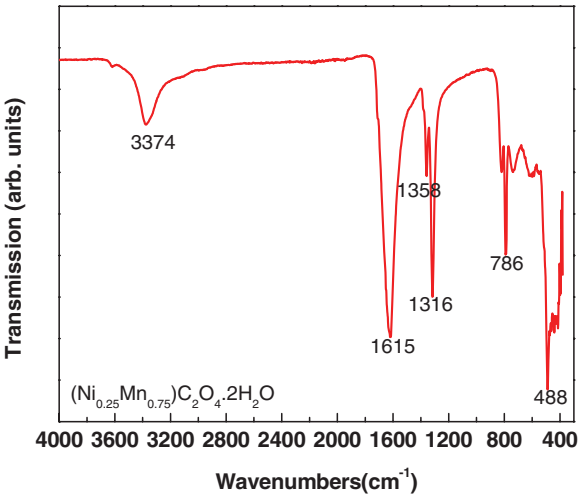

Figure 6. FTIR results of synthesized oxalate precursor.

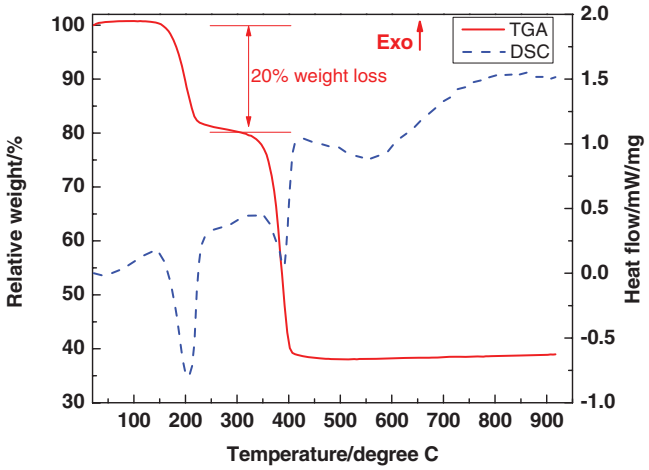

Figure 7. TGA-DSC profile of synthesized oxalate precursor.

lithium addition is necessary to yield the desired lithium-rich composite cathode materials. Between 200 and 300°C, weight loss was about 20%, which corresponds to the release of two structural H_2O from the precursor. This weight loss matches well with the theoretical value of 20.02% when two H_2O are released from $Ni_{0.25}Mn_{0.75}C_2O_4 \cdot 2H_2O$. This weight loss also confirms that the precipitate is di-hydrated transition metal oxalate. The decomposition is complete at around 400°C, with metal oxides and released carbon dioxide gas as the products. The two sharp endothermic peaks at 200°C and 400°C in the DSC plot coincide with the weight losses in the TGA plot. The broad endothermic peak at around 550°C may relate to the partial reduction of Mn^{4+} to Mn^{3+} due to the fact that Mn^{3+} is thermodynamically more stable at high temperature compared to Mn^{4+} (Figure 7).

Precursor prepared at pH 6-7 with ammonia as the pH regulator was chosen for cathode synthesis. After the solid-state reaction between the oxalate precursor and lithium carbonate, a black fine powder was collected. As shown in Figure 8a, synchrotron XRD characterizations were conducted on pristine (oxalate precursor based), ball-milled (oxalate precursor based) and pristine (carbonate precursor based) $Li_{1.5}Ni_{0.25}Mn_{0.75}O_{2.5}$ cathode materials. All these three materials showed typical diffraction patterns of the lithium-rich composite material, which can be mainly indexed as a α-$NaFeO_2$ structure ($R\bar{3}m$), with a secondary component belonging to the Li_2MnO_3-like

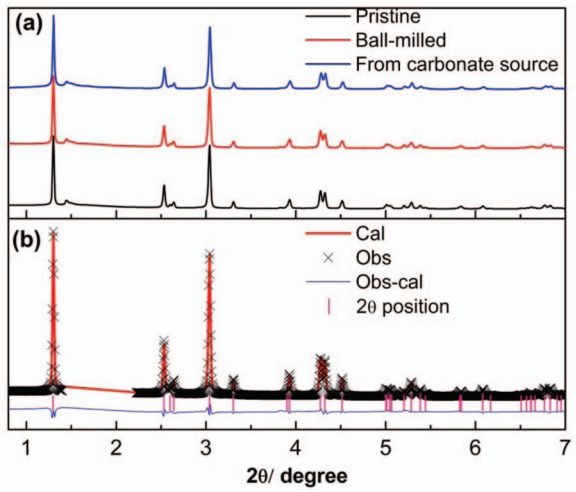

Figure 8 (a) XRD patterns of $Li_{1.5}Ni_{0.25}Mn_{0.75}O_{2.5}$ cathode materials synthesized from oxalate precursor (pristine and ball-milled) and carbonate precursor, (b) XRD Refinement of the oxalate precursor based cathode material.

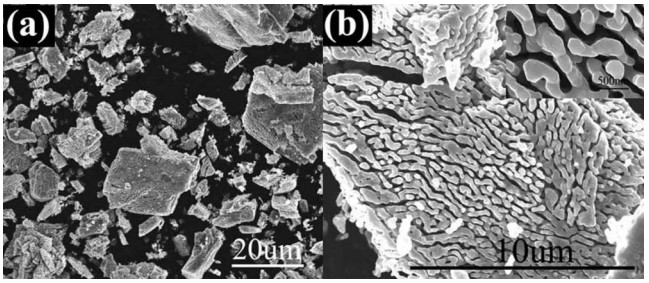

Figure 9. SEM images of $Li_{1.5}Ni_{0.25}Mn_{0.75}O_{2.5}$ cathode material: (a) low magnification; (b) top view with inset image taken at higher magnification.

phase observed between 1.3° and 1.5°. Rietveld refinement was performed on $Li_{1.5}Ni_{0.25}Mn_{0.75}O_{2.5}$ prepared from the oxalate precursor (Figure 8b). The refinement was based on single $R\bar{3}m$ phase model and only Ni/Li disorder was considered. The refined lattice parameters were a = b = 2.861 Å, and c = 14.258 Å, and around 2% Ni was found in the lithium layer, which is consistent with other reports.[16]

The morphology of the synthesized $Li_{1.5}Ni_{0.25}Mn_{0.75}O_{2.5}$ cathode materials was characterized with SEM (Figure 9). The secondary particles had a wide particle size distribution with a plate morphology inherited from the oxalate precursor (Figure 9a). Due to the release of the structural water and carbon dioxide during high temperature calcination, pores with regular patterns were formed among the aligned rod-like primary particles (inset of Figure 9b). These primary particles had an average diameter of approximately 300 nm, and the length was the same as the thickness of the secondary particles (around 5 μm in these synthesis conditions). These features are assumed to benefit the electrochemical reactions of these cathode materials due to the shortened lithium diffusion path length, while the moderate size of the primary particles will not lead to serious parasitic reactions, which are a common problem for nano-sized lithium-rich composite cathode materials.

The cycling and rate performances when tested in CR-2032 lithium cells are shown in Figure 10 and Figure 11, respectively. The current density was C/10, assuming that the 1 C rate is equivalent to 200 mA g^{-1}. The cell was initially charged and discharged within the voltage window of 2–4.8 V for activation, and then operated between 2 and 4.6 V for the subsequent cycles. Stable discharge capacity around 220 mAh $\cdot g^{-1}$ was achieved for up to 70 cycles without capacity degradation (Figure 10). To determine whether the rod-cluster-like

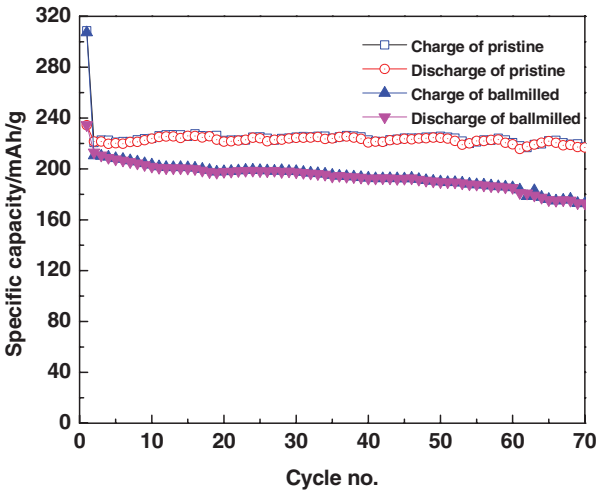

Figure 10. Cycling performance of half cells with $Li_{1.5}Ni_{0.25}Mn_{0.75}O_{2.5}$ cathode material. Tests were conducted under C/10 rate (1C = 200 mA/g) with voltage window of 2–4.6 V.

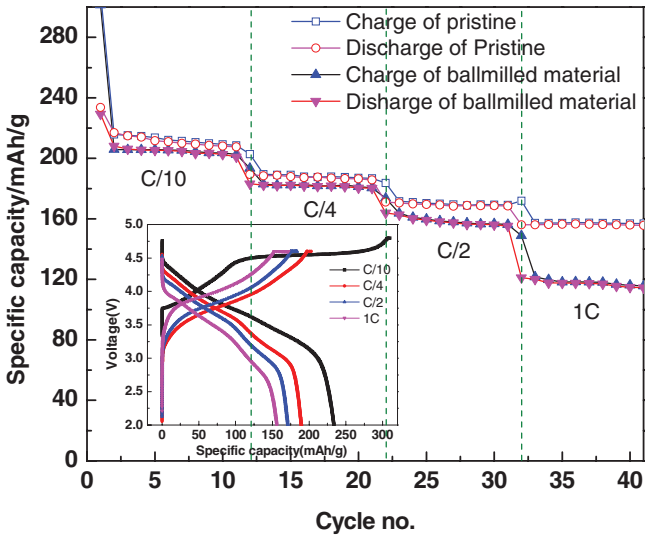

Figure 11. Rate performance of lithium cells with $Li_{1.5}Ni_{0.25}Mn_{0.75}O_{2.5}$ cathode materials (1C = 200 mA/g).

morphology improved the performance, mild mechanical ball milling of the cathode material was conducted for 30 min to break up the structure. The ball-milled materials were tested in the same cell conditions as stated above. The cells displayed similar initial discharge capacity; however, after 70 cycles, the reversible capacity had gradually decreased to 180 mAh $\cdot$ g^{-1} (Figure 10). This comparison highlights the advantage of the rod-cluster-like morphology. The rate capabilities of the material before and after ball milling were also characterized at room temperature with lithium coin cells as shown in Figure 11. Different rates were tested in a sequential manner (C/10, C/4, C/2, and 1C) for ten cycles at each step. At the C/10 and C/4 rates, the materials before and after ball milling show identical capacities of 210 mAh $\cdot$ g^{-1} (C/10) and 185 mAh $\cdot$ g^{-1} (C/4), respectively. However, at C/2, the capacity for the ball-milled material was 15 mAh $\cdot$ g^{-1} lower than that of the pristine one. The difference became as large as 40 mAh $\cdot$ g^{-1} at the 1C rate. This observation is contrary to the conventional belief that smaller particles always endow the material with superior rate performance. Accelerated parasitic reactions may be responsible for the decrease in rate capacity after ball milling. The exact mechanism is still under investigation. The charge-discharge voltage profile at different C rates is shown as an inset in Figure 11. In the first charge, the 4.5 fingerprint voltage plateau for the lithium- manganese- rich cathode material is associated with the electrochemical activation of the Li_2MnO_3-like phase. The voltage profile changed after the first cycle due to the irreversible phase change accompanied with the activation of Li_2MnO_3-like phase.

Conclusions

We synthesized $Ni_{0.25}Mn_{0.75}C_2O_4 \cdot 2H_2O$ with a co-precipitation method to serve as a lithium-manganese-rich cathode precursor. We then conducted a systematic study of the effects of the reaction pH and precipitate agent concentration on the oxalate precursor morphology and composition. When the reaction pH was increased from 1 to 7, the oxalate particles evolved from a cubic to a lamellar morphology. To achieve the target composition, higher pH was necessary when NaOH instead of ammonia was used as the pH regulator. The oxalate precipitates were confirmed as $Ni_{0.25}Mn_{0.75}C_2O_4 \cdot 2H_2O$ after TGA-DSC, XRD, and FTIR characterizations. The synthesized $Li_{1.2}Ni_{0.2}Mn_{0.6}O_2$ cathode material showed a porous morphology among rod-like primary particles. Electrochemical testing of this material in coin cells indicated high and stable capacity (about 220 mAh $\cdot$ g^{-1}) and a superior capacity of the pristine materials compared to that after ball milling to break up the rod-cluster-like morphology.

Acknowledgments

This research was funded by the U.S. Department of Energy, Freedom CAR, and Vehicle Technologies Office. The electron microscopy was accomplished at the Electron Microscopy Center for Materials Research at Argonne National Laboratory, a U.S. Department of Energy Office of Science Laboratory operated under Contract No. DE-AC02-06CH11357 by UChicago Argonne, LLC.

References

1. J.-H. Kim, C. S. Yoon, and Y.-K. Sun, *J. Electrochem. Soc.*, **150**, A538 (2003).
2. Z. Lu and J. R. Dahn, *J. Electrochem. Soc.*, **149**, A815 (2002).
3. C. S. Johnson, J.-S. Kim, C. Lefief, N. Li, J. T. Vaughey, and M. M. Thackeray, *Electrochem. Commun.*, **6**, 1085 (2004).
4. S.-H. Kang, Y. K. Sun, and K. Amine, *Electrochem. Solid-State Lett.*, **6**, A183 (2003).
5. Z. Lu, D. D. MacNeil, and J. R. Dahn, *Electrochem. Solid-State Lett.*, **4**, A191 (2001).
6. T. A. Arunkumar, E. Alvarez, and A. Manthiram, *J. Electrochem. Soc.*, **154**, A770 (2007).
7. Z. Lu, Z. Chen, and J. R. Dahn, *Chem. Mater.*, **15**, 3214 (2003).
8. Y. S. Meng, G. Ceder, C. P. Grey, W.-S. Yoon, and Y. Shao-Horn, *Electrochem. Solid-State Lett.*, **7**, A155 (2004).
9. Y. S. Meng, G. Ceder, C. P. Grey, W.-S. Yoon, M. Jiang, J. Bréger, and Y. Shao-Horn, *Chem. Mater.*, **17**, 2386 (2005).
10. J. Bréger, Y. S. Meng, Y. Hinuma, S. Kumar, K. Kang, Y. Shao-Horn, G. Ceder, and C. P. Grey, *Chem. Mater.*, **18**, 4768 (2006).
11. M. M. Thackeray, S.-H. Kang, C. S. Johnson, J. T. Vaughey, and S. A. Hackney, *Electrochem. Commun.*, **8**, 1531 (2006).
12. M. M. Thackeray, S.-H. Kang, C. S. Johnson, J. T. Vaughey, R. Benedek, and S. A. Hackney, *J. Mater. Chem.*, **17**, 3112 (2007).
13. C. H. Lei, J. Bareño, J. G. Wen, I. Petrov, S.-H. Kang, and D. P. Abraham, *J. Power Sources*, **178**, 422 (2008).
14. J. Bareno, C. H. Lei, J. G. Wen, S. H. Kang, I. Petrov, and D. P. Abraham, *Adv. Mater.*, **22**, 1122 (2010).
15. J. G. Wen, J. Bareño, C. H. Lei, S. H. Kang, M. Balasubramanian, I. Petrov, and D. P. Abraham, *Solid State Ionics.*, **182**, 98 (2011).
16. A. R. Armstrong, M. Holzapfel, P. Novák, C. S. Johnson, S.-H. Kang, M. M. Thackeray, and P. G. Bruce, *J. Am. Chem. Soc.*, **128**, 8694 (2006).
17. S.-H. Park, S.-H. Kang, I. Belharouak, Y. K. Sun, and K. Amine, *J. Power Sources.*, **177**, 177 (2008).
18. D. Wang, I. Belharouak, G. Zhou, and K. Amine, *Adv. Funct. Mater.*, (2012).
19. D. Wang, I. Belharouak, S. Gallagher, G. Zhou, and K. Amine, *J. Mater. Chem.*, **22**, 12039 (2012).
20. G. M. Koenig Jr., I. Belharouak, H. M. Wu, and K. Amine, *Electrochimica Acta.*, **56**, 1426 (2011).
21. D. Wang, I. Belharouak, G. M. Koenig, G. Zhou, and K. Amine, *J. Mater. Chem.*, **21**, 9290 (2011).
22. M.-H. Lee, Y.-J. Kang, S.-T. Myung, and Y.-K. Sun, *Electrochim. Acta*,, **50**, 939 (2004).
23. S.-H. Park, H.-S. Shin, S.-T. Myung, C. S. Yoon, K. Amine, and Y.-K. Sun, *Chem. Mater.*, **17**, 6 (2004).
24. A. van Bommel and J. R. Dahn, *Chem. Mater.*, **21**, 1500 (2009).
25. D. L. Perry and S. L. Phillips, *Handbook of Inorganic Compounds*, CRC Press, 275 (1995).
26. A. Huizing, H. A. M. van Hal, W. Kwestroo, C. Langereis, and P. C. van Loosdregt, *Mat. Res. Bull.*, **12**, 605 (1977).
27. Z. A. D. Lethbridge, A. F. Congreve, E. Esslemont, A. M. Z. Slawin, and P. Lightfoot, *J. Solid State Chem.*, **172**, 212 (2003).
28. B. Małecka, A. Małecki, E. Drożdż-Cieśla, L. Tortet, P. Llewellyn, and F. Rouquerol, *Thermochim. Acta.*, **466**, 57 (2007).
29. S. Guillemet-Fritsch, M. Aoun-Habbache, J. Sarrias, A. Rousset, N. Jongen, M. Donnet, P. Bowen, and J. Lemaître, *Solid State Ionics.*, **171**, 135 (2004).
30. M. A. Gabal, *J. Phys. Chem. Solids.*, **64**, 1375 (2003).